Quasi-Fixed Switching Frequency Control of CRM Boost PFC Converter Based on Variable Inductor in Wide Input Voltage Range

Kai Yao, *Member, IEEE*, Zhen Zhang, Jian Yang, Jintao Liu, Jiazhen Li, and Fanguang Shao

***Abstract*—With traditional constant on-time control, the switching frequency variation range of critical conduction mode boost power factor correction converter is large during a half line cycle, not to mention the wide range of input voltage's rms value. For this issue, this article puts forward a quasi-fixed switching frequency control, which combines the variable on-time and variable inductor technology together. Furthermore, a lower output voltage ripple and a higher efficiency are obtained. In spite of the power factor decrease, the input current harmonics still satisfy the IEC61000-3-2 Class D limits. The detailed theoretical analysis and experimental results are presented in this article.**

***Index Terms*—Critical conduction mode (CRM), power factor correction (PFC), quasi-fixed switching frequency (QFF) control, variable inductor (VI).**

I. Introduction

FOR the improvement of grid power quality and the reduction of line current distortion, power factor correction (PFC) is necessary in ac–dc conversion. Many topologies and control methods of PFC have been put forward for low total harmonics distortion and high power factor (PF) [1], [2]. Critical conduction mode (CRM) boost PFC converters are widely employed in low-to-medium power applications because of its several merits [3]–[5]. Nevertheless, unlike the fixed switching frequency operation manner of a boost PFC converter in continuous conduction mode (CCM) or discontinuous conduction mode (DCM), where the electromagnetic interference (EMI) noises just exist at the multiples of switching frequency, and their maximum values normally happen under the low line and full load, the conducted EMI of a CRM boost PFC converter distributes in wide frequency range, and finding the worst spectrum by repetitive measurements under different input voltage and load conditions are time consuming [6]–[8].

Manuscript received January 21, 2020; revised May 14, 2020; accepted June 21, 2020. Date of publication July 7, 2020; date of current version September 22, 2020. This work was supported in part by the National Natural Science Foundation of China under Grant 51677091 and in part by the Fundamental Research Funds for the Central Universities (30918011331). This paper was presented in part at the IEEE Energy Conversion Congress and Exposition, Baltimore, MD, USA, September–October 2019. Recommended for publication by Associate Editor B. Chen. *(Corresponding author: Kai Yao.)*

The authors are with the School of Automation, Nanjing University of Science and Technology, Nanjing 210094, China (e-mail: yaokai@njust.edu.cn; 690315370@qq.com; yangjian@njust.edu.cn; 397478723@qq.com; 118110022218@njust.edu.cn; az_shao@163.com).

Color versions of one or more of the figures in this article are available online at https://ieeexplore.ieee.org.

Digital Object Identifier 10.1109/TPEL.2020.3007601

It is pointed out in [9] that injecting the appropriate harmonics into the input current can realize variable on-time (VOT) control. With VOT, a constant switching frequency can be achieved during a line cycle, which is in favor of the EMI filter design. However, the constant value of the switching frequency is up to the input voltage's rms value and the switching frequency still varies within wide input voltage range. Since the switching frequency is related to not only the rms input voltage but also the inductance. The idea of adjusting the inductance according to the rms input voltage can be considered, so that fixed switching frequency independent of the input voltage maybe realized. Now, let us focus on the literature on variable inductors (VIs).

A literature review is presented in [10] on magnetically controlled devices, VI, and variable transformers, and their applications to lighting gears for discharge lamps and LED lamps. In [11] and [12], a modeling, simulation, and design approach of VI based on SPICE is proposed, which merges both electrical and magnetic behavior of the VI under any operating conditions. The new structure VI "quad-U" is analyzed in [13] and it provides more reference for the design of VIs. The research in [14] introduces a digitally controlled buck converter with adaptive core biasing that allows for minimization of the output capacitor as well as of the inductor core and improving load transient response. A buck converter is built in [15] for regulating the inductance of main power inductor of power electronic converters. In [16], the VI is used to reduce the switching frequency variation range and improve efficiency. In [17], a novel control scheme with the VI for DCM boost PFC converter is presented. The modeling of the VI and the DCM operation with a VI are derived in detail. The work in [18] puts forward a single-stage flyback PFC circuit with variable boost inductance for high-brightness LED applications for the universal input voltage. The boost inductance has a constant high value at high line, whereas at low line, it is reduced proportionally to the load current, so that the line-current harmonic limits are satisfied. A VI-based LED driver for dc grid lighting applications is proposed in [19]. By introducing a VI as the series inductor, the LED current can be controlled independently from any other parameter, which makes it possible to drive and regulate several LED branches from the same half-bridge output.

In this article, a control scheme is proposed to achieve fixed switching frequency for a CRM boost PFC converter in wide input voltage range. The operating principle of the CRM boost converter and the VI are showed in Section II. In Section III,

the operating principle of the quasi-fixed switching frequency (QFF) control is analyzed, and the VI is designed and the corresponding control method is put forward. In Section IV, the performance comparison between the proposed method and the traditional control is made in terms of the switching frequency, the peak and rms current of the inductor, and the output voltage ripple. Section V shows experimental results. The waveforms of the input current, inductor current, and the output voltage in line cycles and switching cycles are presented. The input current harmonics are tested by the power analyzer. The measured switching frequency, the efficiency, the output voltage ripple, and the PF are given. The transient response of the inductor current and output voltage with load and input voltage step change are shown in line cycles and switching cycles, respectively. The EMI spectra and the attenuation requirement (AR) of the converter are recorded. The phenomenon that the inductor current does not rise or fall linearly in switching cycles is explained. At the same time, the real-time inductance as a function of the bias current and the main current is derived. Finally, Section VI concludes this article.

II. Operating Principle of a CRM Boost PFC Converter and VI

A. Operating Principle of a CRM Boost PFC Converter

The specific operation principle and detailed formula derivation process have been given in [9]. The input voltage, the inductor peak current, the input current, the ON-time, and the switching frequency are expressed in

$$v_{\text{in}} = v_g = V_m \sin \omega t \tag{1}$$

$$i_{Lb\_pk} = \frac{v_g}{L_b} t_{\text{ON}} = \frac{V_m \left|\sin \omega t\right|}{L_b} t_{\text{ON}} \tag{2}$$

$$i_{\text{in}} = \frac{V_m \sin \omega t}{2L_b} t_{\text{ON}} \tag{3}$$

$$t_{\text{ON}} = \frac{4L_b P_o}{V_m^2} \tag{4}$$

$$f_s = \frac{1}{t_{\text{ON}}} \left(1 - \frac{V_m}{V_o} \left|\sin \omega t\right|\right) = \frac{V_m^2}{4L_b P_o} \left(1 - \frac{V_m}{V_o} \left|\sin \omega t\right|\right) \tag{5}$$

where V_m is the amplitude of the input voltage, ω is the angular frequency of the input voltage, and V_o is the output voltage.

According to (5) and the parameters of the converter in Section V, we can get the variation curves of the switching frequency in a half line cycle with COT, as shown in Fig. 1. It can be clearly seen that the switching frequency varies in a wide range, especially at high input voltages. The minimum and maximum values at 90, 176, and 264 VAC are 35.7 and 52.3, and 75.6 kHz, and 200.1, 30, and 450.2 kHz, respectively.

B. Operating Principle of a VI

Fig. 2 demonstrates the basic model schematic of the VI with double E core. The main inductor winding N_L is wound on the

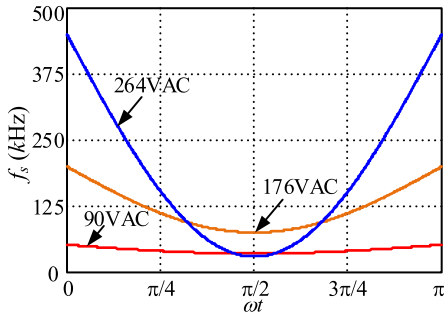

Fig. 1. Switching frequency curves in a half line cycle with COT.

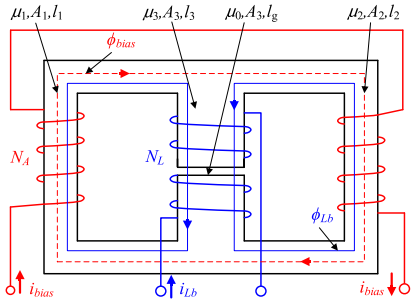

Fig. 2. VI using a double E core.

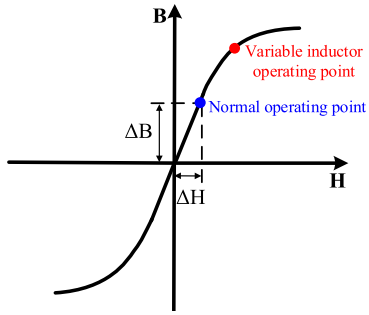

Fig. 3. Hysteresis curve.

air-gapped center leg and the auxiliary winding N_A is wound on the outer legs.

When i_{Lb} flows through N_L, a main magnetic flux ϕ_{Lb} is produced and it flows through both the center leg path and the outer path. If a bias current i_{bias} flows through N_A, a bias magnetic flux ϕ_{bias} is produced along the outer path of the double E core, instead of the center leg due to the airgap. Consequently, the main inductor L_{b_var} is influenced not only by the permeability of the center leg path, but also by the outer path. Or rather, the bias current i_{bias} reduces the permeability of the outer path, resulting in the reduction of the main inductance L_{b_var}.

Actually, the bias current i_{bias} pushes the operating point on the *B–H* curve toward the nonlinear saturation region, as shown in Fig. 3. The accurate design and theoretical analysis are detailed in [20] and L_{b_var} can be expressed as follows:

$$L_{b\_\text{var}} = \left[\frac{l_1}{2\mu_0 \mu_{\text{var}} A_1 n_3^2} + \frac{l_3}{\mu_0 \mu_3 A_3 n_3^2} + \frac{l_g}{\mu_0 A_3 n_3^2}\right]^{-1} \tag{6}$$

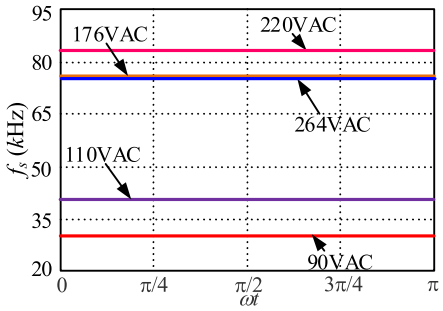

Fig. 4. Switching frequency curves in a half line cycle with VOT.

where μ_0 is the permeability of air and $\mu_{1=}\mu_{2=}\mu_{\rm var}$ and μ_3 are the relative permeability of the outer path and the center leg path, respectively. A_1 and A_3 are the area of the outer leg and center leg, respectively. l_1, l_3, and l_g are the lengths of the half outer core path, the center leg core path, and the air gap path, respectively.

III. Quasi-Fixed Switching Frequency (QFF) Control Based on VI

A. Derivation of Quasi-Fixed Switching Frequency Control Based on a VI

It can be observed from (5) that if the ON-time of the switch varies as follows, then the switching frequency during a half line cycle is constant:

$$t_{\rm ON} = T_s\left(1 - \frac{V_m}{V_o}|\sin\omega t|\right) \tag{7}$$

where T_s is an undetermined coefficient, which will be calculated afterward.

Based on the power balance between the input and output, the input power can be expressed as

$$P_{\rm in} = P_o = \frac{1}{\pi}\int_0^{\pi} v_{\rm in} i_{\rm in} d\omega t = \frac{T_s V_m^2}{2L_b}\left(\frac{1}{2} - \frac{4V_m}{3\pi V_o}\right). \tag{8}$$

From (8), the switching frequency with VOT is derived as

$$f_s = \frac{1}{T_s} = \frac{V_m^2\left[1/2 - (4V_m/3\pi V_o)\right]}{2P_o L_b}. \tag{9}$$

Selecting a minimum switching frequency $f_{s\_\min}$, we can get the inductor from (9) as

$$L_{b\_\max} = \frac{V_m^2\left[1/2 - (4V_m/3\pi V_o)\right]}{2P_o f_{s\_\min}}. \tag{10}$$

To keep the minimum switching frequency above 30 kHz, the critical inductor value is 821 μH over a wide input voltage range under VOT. With this inductance, curves of the switching frequency in a half line cycle with VOT can be plotted in Fig. 4. Obviously, the switching frequency is constant during a half line cycle. However, the constant switching frequency value still changes with the input voltage's rms value. This is a problem that needs to be solved.

In order to achieve constant frequency in a wide input voltage range, firstly, it is necessary to use VOT to achieve a constant switching frequency at a certain input voltage. Then, the inductor value can be adjusted by the VI technology to make the switching frequency constant over the wide input voltage range.

According to (10) and $f_{s\_\min} = 30$ kHz, $P_o = 120$ W, and $V_o = 400$ V, the critical inductance under the input voltages of 90, 110, 220, and 264 is 0.821, 1.126, 2.284, and 2.011 mH, respectively. In other words, by adjusting the inductance according to the rms value of the input voltage, the switching frequency with VOT control can be kept constant over the wide input voltage range.

B. Control Circuit of Quasi-Fixed Switching Frequency Control Based on VI

The control implementation is demonstrated in Fig. 5, where a digital signal processor (DSP) TMS320F28377D is adopted in feed-forward circuit and the VI control circuit.

The output voltage V_o and the peak value of the rectified input voltage V_m are sent into DSP by analog-to-digital converter (ADC). v_{Ecap1} is the signal for a DSP to realize phase lock. Through the zero-crossing comparator in a phase-locked circuit, the input voltage $v_{\rm in}$ is turned into pulsewidth modulation voltage v_{Ecap1}, whose rising edge and falling edge is synchronized with the zero-crossing instant of the input voltage. In this way, a DSP can build a sinusoidal function with the same initial phase and frequency as that of the input voltage. By the envelope generation unit, which includes the subtraction, multiplication, and division, the inductor current peak envelope signal of $kV_m|\sin\omega t|(1 - V_m|\sin\omega t|/V_o)$can be generated, where k is the sampling coefficient of the input voltage and output voltage. $v_{\rm driver}$ is the driving signal of the switch. Through a wave shaping circuit, the basic shape of v_{Ecap2} is the same as with $v_{\rm driver}$, however, the noises are removed, and the rising edge and the falling edge are steeper. The rising edge of v_{Ecap2} can be captured by Ecap2. Consequently, the switching frequency can be obtained by the frequency calculation unit. It should be noted that it is not necessary to continuously sample and calculate the frequency of every switching cycle. However, In order to improve the accuracy, the switching frequency values at multiple instants in line cycle should be sampled and the data need to be averaged. The DSP TMS320F28377D is adopted and it provides 200-MHz signal processing performance and the time resolution of the ECAP module can achieve 5 ns, which is enough to sample the switching frequency. In addition, PI regulation, phase lock, sampling of input and output voltages, generation of envelope, and digital-to-analog conversion are not very complex operations, which do not need to occupy too much DSP resources. Therefore, even for a higher switching frequency greater than 100 kHz, the calculation speed is enough.

The switching frequency is compared with the reference frequency $f_{\rm ref}$ in the PI adjustment unit and an error $v_{\rm ea}$ is yielded. Then, the error is converted to the bias voltage v_{DAC2} by a DAC. If the frequency is higher than 30 kHz, the bias voltage will decrease and so does the bias current. Correspondingly, the variable inductance will increase and the switching frequency will decrease. The whole regulating process lasts till that the switching frequency is $f_{\rm ref} = 30$ kHz. If a step change occurs in the input voltage or the load, this process is carried out simultaneously with the adjustment of the output voltage. Obviously,

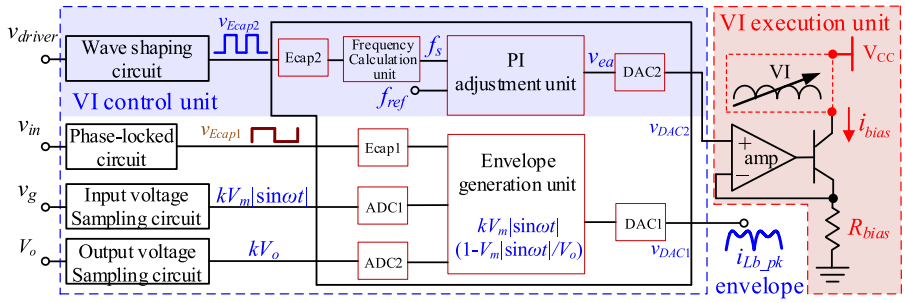

Fig. 5. ON-time and variable inductance control circuit for a CRM boost PFC converter with QFF.

the time required to stabilize the final inductance is limited by the adjustment time of the output voltage, for the bandwidth of the output voltage loop is low.

Considering that the maximum output current of general-purpose input and output (GPIO) is only 10 mA, which is far less than the necessary bias current value, we build a voltage-controlled current source (VCCS) with the operational amplifier and the triode. The bias current can be calculated by $i_{\rm bias} = v_{DAC2}/R_{\rm bias}$. It should be noted that a higher value of $R_{\rm bias}$ means a higher addition power loss, whereas a lower value demands a higher accuracy of the GPIO output. Finally, $R_{\rm bias} = 0.5\ \Omega$ is adopted.

C. Design and Measurement of a VI

With COT, in order to ensure that the switching frequency is higher than the lowest frequency of 30 kHz at any input line angle over the wide input voltage range, the critical inductance is designed as $L_{\rm COT} = 645\ \mu$H. Considering the characteristics of the VI, the inductance value decreases as the bias current increases. Therefore, when designing the critical inductor value with QFF, the maximum critical inductance value corresponding to 220 VAC is selected as $L_{QFF1} = 2284\ \mu$H and $L_{QFF2} = 686\ \mu$H at 30 and 100 kHz, respectively.

The filling factor K_u can be expressed as where N_b and S are turns number and sectional area of the winding, respectively.

$$K_\mu = \frac{N_b S}{A_w} = \frac{L_b N_{Lb\_pk\_\max} I_{Lb\_\rm rms\_\max}}{\Delta B A_w A_e J}. \tag{11}$$

where $I_{Lb\_pk\_\max}$ and $I_{Lb\_\rm rms\_\max}$ are the maximum peak and rms value of the inductor current, respectively. ΔB is the flux density, A_e and A_w are, respectively, the effective area and window area of the magnetic core, and J is current density.

Assuming the wire is wound uniformly, the copper volume required for the inductor design can be considered as

$$V_{\rm copper} = \pi d N_L S \tag{12}$$

where d is the diameter of the leg.

To be fair, the inductors under two different control methods are made with the same core in the laboratory. The specific design parameters are listed in Table I. Obviously, if the constant switching frequency is 30 kHz, the filling factor and the copper's volume are a little higher than that with COT. However, if the frequency is 100 kHz, there is almost no difference between them. Therefore, the additional size and cost of the VI depends on the designed constant switching frequency.

TABLE I
INDUCTOR PARAMETERS UNDER TWO CONTROLS

Items		Conventional method	Proposed method	
Boost Inductor	Core	ETD29		
		L_{COT}=645μH	L_{QFF1_max}=2284μH L_{QFF1_min}=821μH	L_{QFF2_max}=686μH L_{QFF2_min}=247μH
	Wire	Main winding: 0.1Φ×20	Main winding: 0.1Φ×20 Aux. winding: 0.2Φ	
		N_L=103	N_L=161 N_A=140	N_L=103 N_A=43
	Air gap	δ=1.57mm	δ=1.08mm	δ=1.46mm
	Filling factor	0.217	0.373	0.227
	Copper's Volume	0.942cm^3	1.483cm^3	0.944cm^3

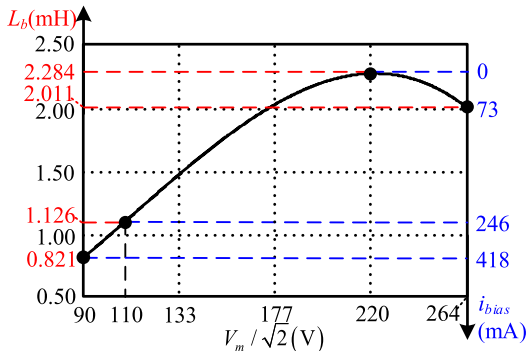

Fig. 6. Curve of critical inductance and bias current in wide input voltage range.

After making the VI, in order to confirm the relationship between the inductance and the bias current, a measurement experiment was performed in the laboratory. With the HIOKI IM3536 LCR meter and the ITECH IT6302 dc power supply, we make some tests on the inductor by injecting bias currents into the auxiliary winding while keeping the main winding current at zero. For achieving the required inductance at different input voltages, the corresponding bias current values can be obtained and the curve is plotted in Fig. 6. It can be seen that the bias currents under the input voltages of 90, 110, 220, and 264 VAC are 418, 246, 0, and 73 mA, respectively.

IV. PERFORMANCE COMPARISON

A. Variation Range of Switching Frequency

According to (5), (9), and the parameters of the converter in Section V, we can draw the switching frequency curves in a half

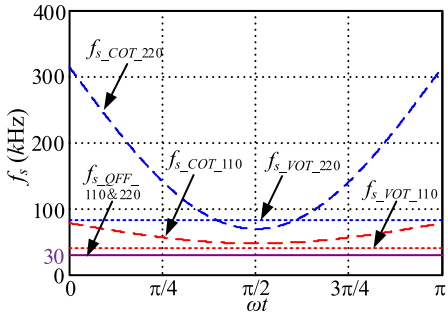

Fig. 7. Switching frequency in a half line cycle with three control schemes.

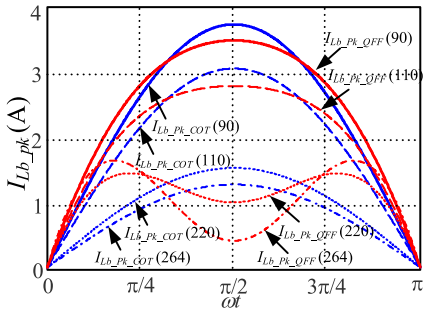

Fig. 8. Waveforms of the inductor peak current.

line cycle at the nominal input voltages of 110 and 220 VAC, as shown in Fig. 7. It can be seen that the switching frequency varies in a wide range with COT. Under VOT control, the switching frequency is constant during a half line cycle. But the constant switching frequency value still changes with the input voltage's rms value. At the same time, we can observe that the proposed QFF control makes the switching frequency fixed at the critical value 30 kHz over the wide input voltage range. The new control method combines VOT control and VI technology to achieve the true constant switching frequency in wide input voltage range.

B. Peak and RMS Current of Inductor

From (2) and (4), the inductor peak current of the converter with COT can be derived as

$$i_{Lb\_pk\_\mathrm{COT}} = \frac{4P_o}{V_m}\left|\sin\omega t\right|. \tag{13}$$

Combining (9) with (19) yields the ON-time of QFF

$$t_{\mathrm{ON}} = \frac{2P_oL_b}{V_m^2\left[1/2-(4V_m/3\pi V_o)\right]}\left(1-\frac{V_m}{V_o}\left|\sin\omega t\right|\right). \tag{14}$$

Substituting (14) into (2) yields the inductor peak current with QFF that can be expressed as

$$i_{Lb\_pk\_\mathrm{QFF}} = \frac{2P_o\sin\omega t}{V_m\left[1/2-(4V_m/3\pi V_o)\right]}\left(1-\frac{V_m}{V_o}\left|\sin\omega t\right|\right). \tag{15}$$

The peak current curves are shown in Fig. 8, which demonstrates that QFF achieves a lower value around $\pi/2$ and a higher value around 0 and π at high input voltages, compared to that with COT.

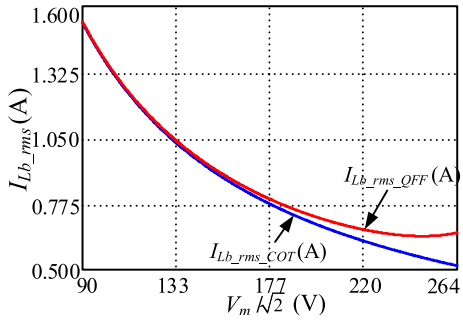

Fig. 9. RMS value of the inductor current.

In a half line cycle, the current's rms value of the inductor with COT and QFF is presented as follows:

$$I_{Lb\_\mathrm{rms\_COT}} = \frac{2\sqrt{2}}{\sqrt{3}}\frac{P_o}{V_m} \tag{16}$$

$$I_{Lb\_\mathrm{rms\_QFF}} = \frac{2P_o\sqrt{\int_0^{\pi}\left[\sin\omega t\left(1-\frac{V_m}{V_o}\left|\sin\omega t\right|\right)\right]^2 d\omega t}}{\sqrt{3}\pi V_m\left[1/2-(4V_m/3\pi V_o)\right]} = \frac{2P_o\sqrt{1/2-(8V_m/3\pi V_o)+3{V_m}^2/8{V_o}^2}}{\sqrt{3}V_m\left[1/2-(4V_m/3\pi V_o)\right]}. \tag{17}$$

Based on (16) and (17), Fig. 9 is plotted, which indicates that QFF obtains nearly the same rms value as that with COT, especially under a low input voltage.

C. Reduction of Output Voltage Ripple

From (1) and (3), the instantaneous input power with COT can be derived as

$$p_{\mathrm{in\_COT}} = v_{\mathrm{in}}i_{\mathrm{in\_COT}} = 2P_o\sin^2\omega t. \tag{18a}$$

Under QFF control, the input current is half of the peak inductor current. Based on (3) and (15), the instantaneous input power with QFF can be expressed as

$$p_{\mathrm{in\_QFF}} = v_{\mathrm{in}}i_{\mathrm{in\_QFF}} = \frac{P_o\sin^2\omega t}{1/2-(4V_m/3\pi V_o)}\left(1-\frac{V_m}{V_o}\left|\sin\omega t\right|\right). \tag{18b}$$

Fig. 10 can be plotted according to 18(a) and 18(b). When $p_{\mathrm{in}}>1$, the output capacitor C_o is charged, and when $p_{\mathrm{in}}<1$, C_o is discharged. t_1 and t_2 are the time instants when p_{in1} and p_{in2} cross 120 W for the first time in a half line cycle, respectively.

Under COT and QFF control, the powers on the output capacitor, respectively, are as follows:

$$p_{C\_\mathrm{COT}}(t) = p_{\mathrm{in\_COT}}(t) - P_o = 2P_o\sin^2\omega t - P_o \tag{19a}$$

$$p_{C\_\mathrm{QFF}}(t) = p_{\mathrm{in\_QFF}}(t) - P_o = \frac{P_o\sin^2\omega t}{1/2-(4V_m/3\pi V_o)}\left(1-\frac{V_m}{V_o}\left|\sin\omega t\right|\right) - P_o. \tag{19b}$$

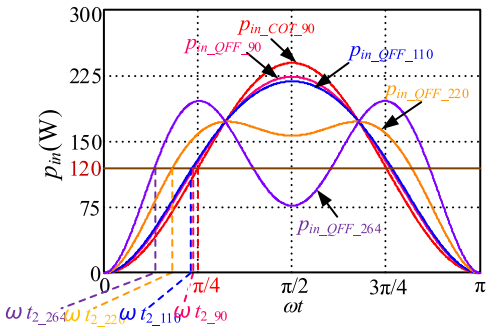

Fig. 10. Instantaneous input power in a half line cycle with COT and QFF.

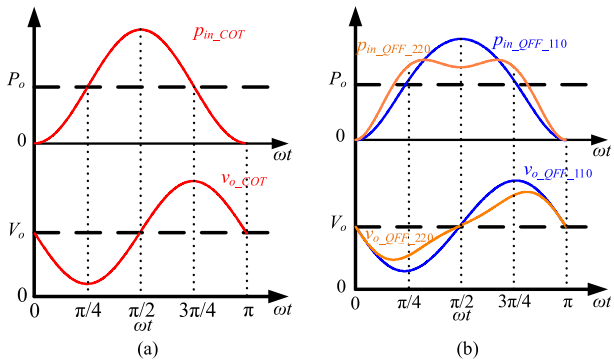

Fig. 11. Instantaneous power and instantaneous voltage on the output capacitor. (a) Under COT control. (b) Under QFF control.

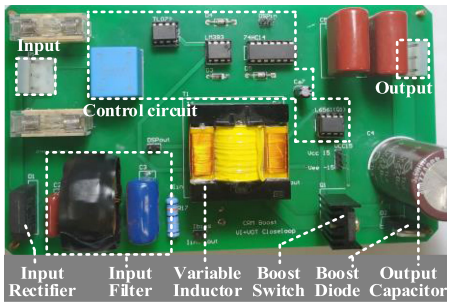

Fig. 12. Experimental prototype.

Equations (19) can be adopted to calculate the instantaneous output voltage and the results are depicted in Fig. 11, which demonstrates that COT obtains a stable voltage ripple under different input voltages, and QFF realizes a lower value. As the input voltage increases, the output voltage ripple decreases obviously. In other words, if the maximum output voltage ripple remains the same, the output capacitor can be reduced. It is beneficial to increase power density because electrolytic capacitors typically occupy a considerable size and volume.

V. Experimental Verification

In order to verify the effectiveness of the theoretical analysis, a prototype has been built and tested in the lab, as shown in Fig. 12. The specifications are listed in Table II. The main component parameters of the prototype are as follows: the power switch Q_b: FQPF4N60C(600V/4A); the boost diode D_b: MUR560(600 V/5 A/1.5 V); the output filter.

TABLE II
Specifications of Prototype

Input voltage	Output voltage	Output power	Minimum switching frequency
90~264 VAC / 50 Hz	400 VDC	120W	30 kHz

Capacitance: $C_o = 220\ \mu$F; and the boost inductances: $L_{\rm COT} = 645\ \mu$H and $L_{\rm QFF} = 2284\ \mu$H.

The experimental waveforms of the input voltage, the input current, the boost inductor current, and output voltage ripple at 110 and 220 VAC with the two control schemes are displayed in Figs. 13(a), 14(a), 15(a), and 16(a), respectively. The waveforms of the input current and inductor peak current are sinusoidal with COT. With QFF, there are some distortions in the currents. The tested input current harmonics are recorded by the power analyzer YOKOGAWA WT1800, as shown in Fig. 17. It can be noticed that the third and third harmonics are dominant. A higher input voltage with QFF requires more harmonic contents. In addition, all the harmonics are lower than the limits of IEC 61000-3-2 Class D.

The waveforms of the inductor current expanded around $\omega t = 0$ and $\omega t = \pi/2$, at 110 and 220 VAC under two control schemes, are given in Figs. 13(b) and (c) and 16(b) and (c). Obviously, the switching frequency of the converter with COT varies not only in a half line cycle, but also with the rms input voltage. By contrast, QFF control achieves a nearly fixed value of 30 kHz in a half line cycle during a wide input voltage range.

Fig. 18 exhibits the measured switching frequency during a half line cycle.

Fig. 19 illustrates the experimental results of efficiency, and QFF can achieve higher efficiency compared with COT. As can be seen from Fig. 32 in Appendix, the efficiency improvement is mainly attributed to the reduction of switching loss, inductor core loss, and coil loss. Obviously, (A6) and (A7) in Appendix exhibits that a lower switching frequency or a higher inductance result in a lower switching turn-OFF loss.

As can be seen from (A10) and (A11), since the same core is adopted for the two methods, the switching frequency and the swing of flux density are the main factors affecting the core loss. Although the switching frequency with QFF is lower than that with COT, the maximum flux density with QFF at 115-VAC input is basically the same as that with COT, whereas the maximum flux density with QFF at 230 VAC is larger than that with COT. Consequently, the reduction of core loss at 115-VAC input is greater than that at 230 VAC.

Fig. 9 indicates that the rms value of inductor current with COT is slightly lower than that with QFF, especially when the input voltage is high. However, the resistance value of the inductance is relatively large at high frequency, as can be seen from Fig. 31. Therefore, the coil loss with COT is higher than that with QFF.

Actually, the bias winding will produce some additional conduction loss. Yet, the resistor in the voltage-controlled current source is only 0.5 Ω and the resistance of the bias winding

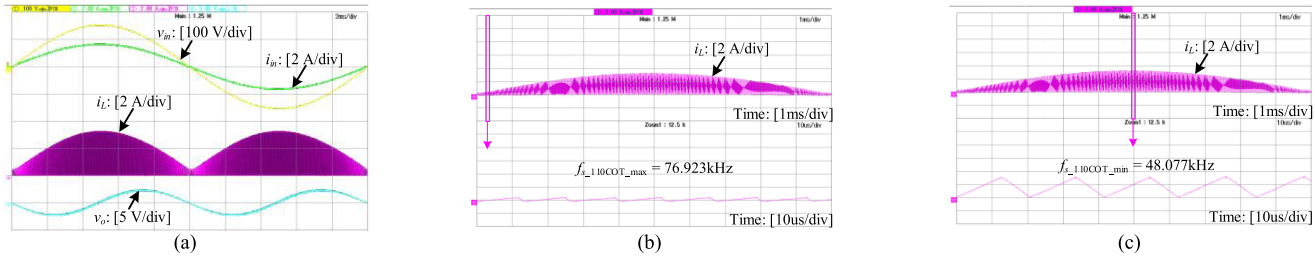

Fig. 13. Experimental waveforms with COT when $v_{\rm in} = 110$ VAC. (a) Measured input voltage, input current, inductor current, and output voltage ripple in line cycle. (b) Inductor current expands at $\omega t = 0$. (c) Inductor current expands at $\omega t = \pi/2$.

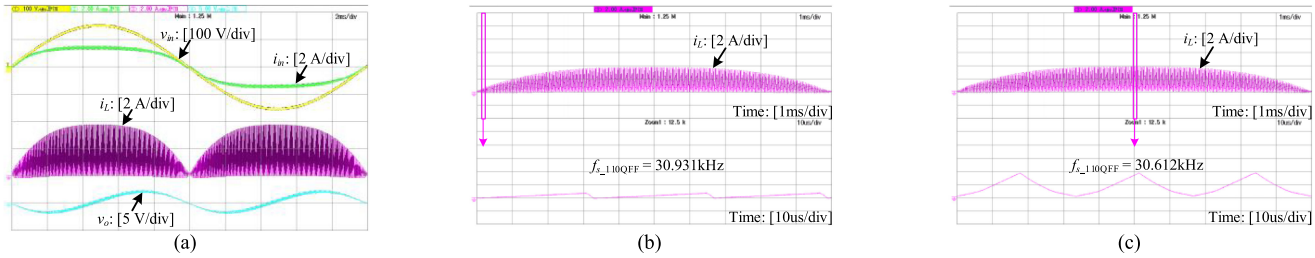

Fig. 14. Experimental waveforms with QFF when $v_{\rm in} = 110$ VAC. (a) Measured Input voltage, input current, inductor current, and output voltage ripple in line cycle. (b) Inductor current expands at $\omega t = 0$. (c) Inductor current expands at $\omega t = \pi/2$.

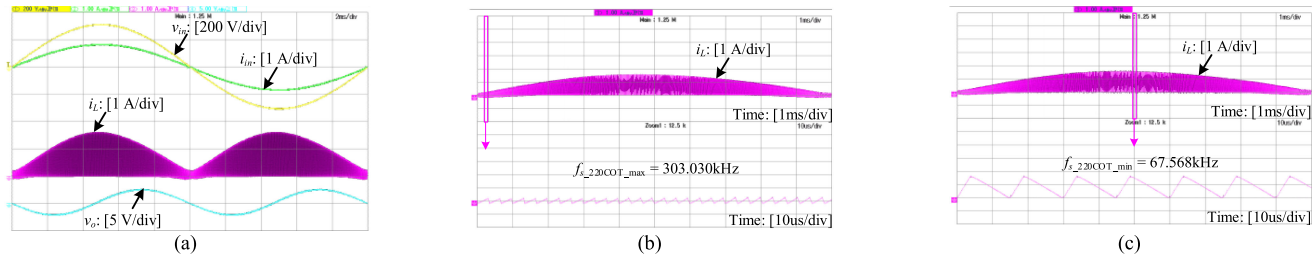

Fig. 15. Experimental waveforms with COT when $v_{\rm in} = 220$ VAC. (a) Measured input voltage, input current, inductor current, and output voltage ripple in line cycle. (b) Inductor current expands at $\omega t = 0$. (c) Inductor current expands at $\omega t = \pi/2$.

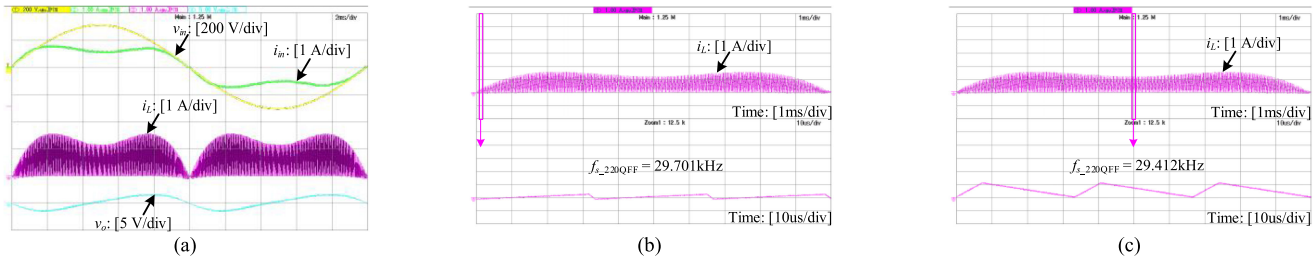

Fig. 16. Experimental waveforms with QFF when $v_{\rm in} = 220$ VAC. (a) Measured input voltage, input current, inductor current, and output voltage ripple in line cycle. (b) Inductor current expands at $\omega t = 0$. (c) Inductor current expands at $\omega t = \pi/2$.

is 2.5 Ω. As shown in Fig. 6, this loss is quite low even in the case of maximum bias current.

The tested output voltage ripple is exhibited in Fig. 20, which indicates that QFF brings about a lower ripple value, especially when the input voltage is high.

Fig. 21 illustrates the experimental results of PF. It can be noticed that QFF obtains a lower PF than that with COT, especially under a high input voltage.

It is worth noting that the shape of inductor current is not straight in switching cycles with QFF control at 110 VAC,

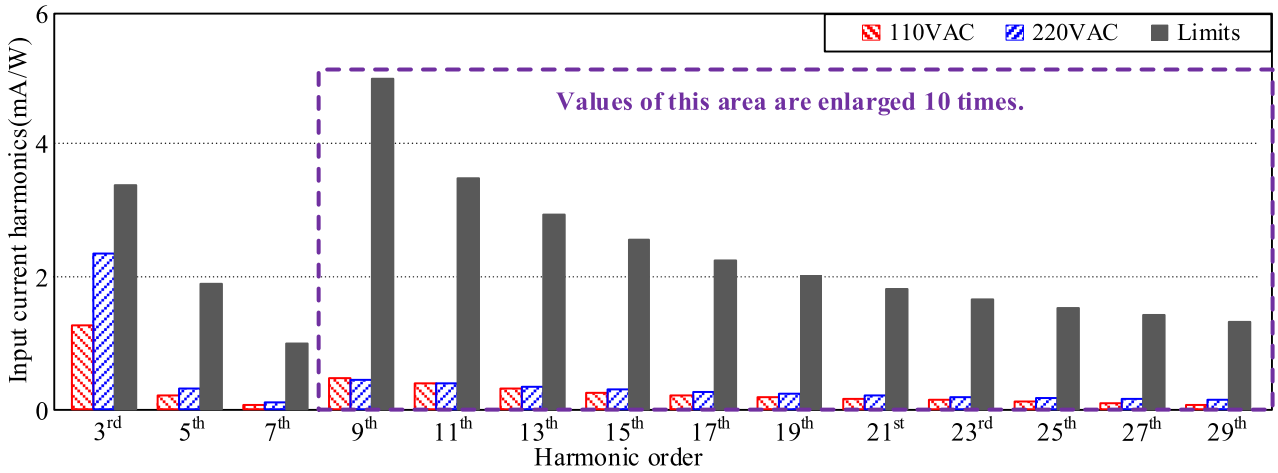

Fig. 17. Experimental results of input current harmonics with QFF.

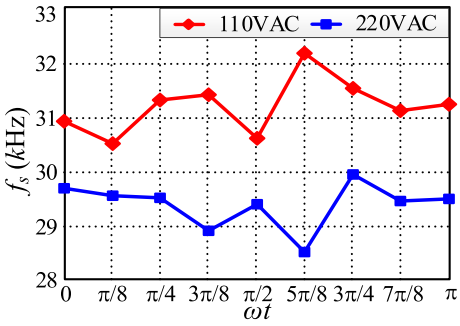

Fig. 18. Measured switching frequency during a half line cycle.

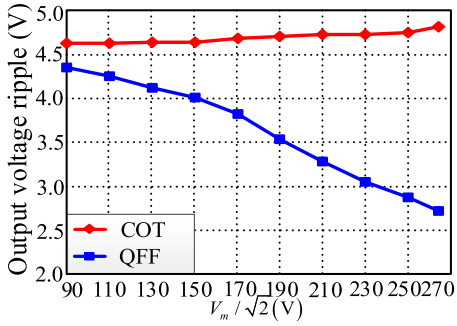

Fig. 20. Measured output voltage ripple.

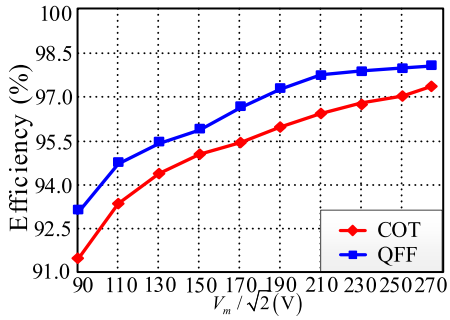

Fig. 19. Experimental results of efficiency.

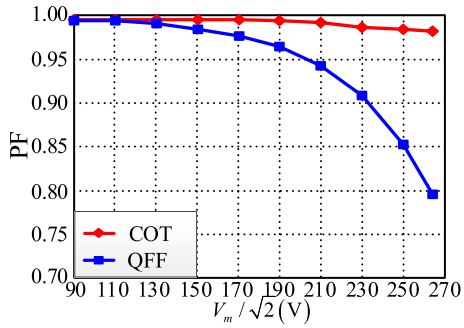

Fig. 21 Experimental results of PF.

which is explained as follows. In this case, the bias current is relatively high and the operating point of the VI is closer to nonlinear saturation region. Consequently, the inductance is somehow influneced by the main inductor current. Fig. 22 shows a step-by-step method to derive the expression of the variable inductance L_{b_var} as a function of the bias current i_{bias} and the main inductor current i_L.

Step I: Taking $v_{\mathrm{in}} = 110$ VAC and $\omega t = \pi/2$ as an example, 20 sets of the instantaneous vaule of the main inductor current and the corresponding time instant in the rising period within a switching cycle can be measured and recorded by the oscilloscope.

Step II: The fitted function of i_L regarding the time t can be got with these data.

Step III: From $L_b = v_{\mathrm{in}}/(di_L/dt)$, the instantaneous inductance as a function of the time t is obtianed.

Step IV: The relationship curve between the instantaneous inductance and i_L can be achieved from the results of II and III. The inductance deceases with the increase in i_L and the initial value at $i_L = 0$ is nearly the same as that in Fig. 4.

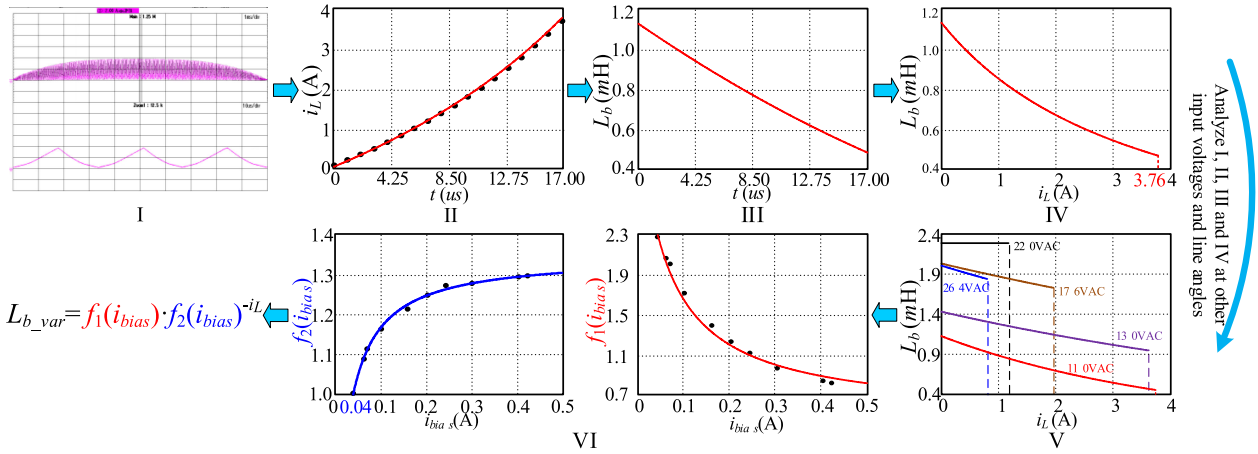

Fig. 22. Flowchart of experimental method to derive the function $L_{b\_\mathrm{var}}(i_{\mathrm{bias}}, i_L)$.

Fig. 23. Transient response of the inductor current with QFF under the input voltage step change between 220 and 176 VAC at 100% load. (a) Around the step change point. (b) In switching cycles during the two stable operation.

Interestingly, the curve can be expressed by an exponential function 1.126×1.274^{-iL}. It should be noted that, through detailed analysis and integral verification, we find that this function is also applicable for the switching cycles at other line angles of 110-VAC input, and the only difference is the peak current and the corresponding minimum inductance in a switching cycle.

Step V: Conducting the same analysis as step I to step IV under different input voltages results in a series of exponential functions.

Step VI: The coefficients and bases of these functions can be fitted into two functions $f_1(i_{\mathrm{bias}})$ and $f_2(i_{\mathrm{bias}})$, respectively, where i_{bias} is got from the actual prototype operation. Therefore, we obtain the following:

$$L_{b\_\mathrm{var}}(i_{\mathrm{bias}}, i_L) = f_1(i_{\mathrm{bias}}) \cdot [f_2(i_{\mathrm{bias}})]^{-i_L} = \left(\frac{0.29 i_{\mathrm{bias}} + 0.34}{i_{\mathrm{bias}} + 0.113}\right)\left(1.35 - \frac{0.023}{i_{\mathrm{bias}} + 0.026}\right)^{-i_L}. \quad (20)$$

If the abovementioned analysis is conducted based on the falling period in switching cycles, we can get almost the same results as (20). The slight difference comes from the hysteresis.

To clarify, (20) is obtained from the experimental data and oriented toward a specific inductor, which is reflected by the constants in (20). Further investigation is needed to obtain a complete expression demonstrating the relationship between the inductance and the number of turns n, the area of leg A, the length of core path l, and the permeability μ, besides i_{bias} and i_L.

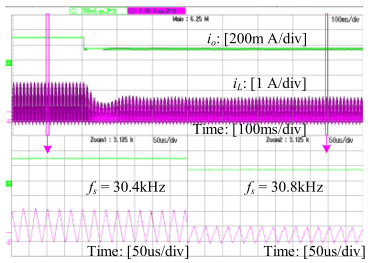

Fig. 24. Transient response of the inductor current with QFF under the load step change at 130 VAC.

Fig. 23 shows the transient response of the inductor current with QFF under the input voltage step change between 220 and 176 VAC at 100% load. Under the QFF control, there is no bias current at 220 V, and the VI control circuit should provide a certain bias current at 176 V to reduce the inductance, thereby adjusting the switching frequency to 30 kHz. When the input voltage changes from 220 to 176 V, on the one hand, the corresponding input voltage sampling circuit in Fig. 5 will adjusts V_m to change the peak current envelope shape, as shown in Fig. 23(a), which the inductor current envelope is different

Fig. 25 Transient response of the output voltage with the load step change at 220 VAC. (a) With COT. (b) With QFF.

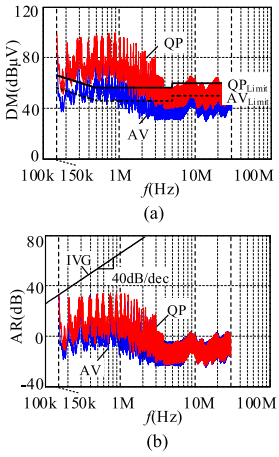

Fig. 26. Experimental results at 220 VAC with QFF. (a) DM noise spectrum. (b) AR.

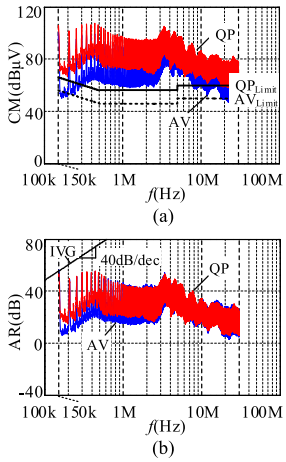

Fig. 27. Experimental results at 220 VAC with QFF. (a) CM noise spectrum. (b) AR.

before and after the input voltage step change. On the other hand, the switching frequency will vary due to the input voltage step change, so the frequency detection unit samples the real-time frequency, then the PI adjustment unit adjusts $v_{\rm ea}$ according to the real-time frequency, so as to obtain the suitable bias current to stabilize the switching frequency at $f_{\rm ref} = 30$ kHz. It can be seen from Fig. 23(a) that the above adjustment process lasts about five line cycles. At the same time, Fig. 23(b) illustrates that the above closed loop can effectively adjust the switching frequency to 30 kHz in the case of input voltage step change.

Fig. 24 gives the transient response of the inductor current with QFF under the load step change at 130 VAC. It can be noticed that the VI control unit also worked well to regulate the bias current to stabilize the switching frequency at 30 kHz when the load changes.

Fig. 25 records the transient response of the output voltage with the load step change at 220 VAC. Obviously, the QFF has no effective improvement on the transient response, because the bandwidth of the output voltage control loop should be far less than the double line frequency.

For discovering the effect of the QFF scheme on the EMI, the tests are conducted on the converter under various inputs, with COT and QFF. No EMI filter is installed and the noise spectrum under 220 VAC is presented.

Figs. 26 and 27 demonstrate that the noises are predominately located in nearly 150, 180, 210, 240, 270, 300 kHz, etc., which actually are the multiplication of the controlled fixed switching

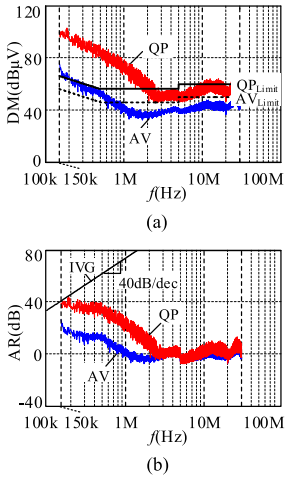

Fig. 28. Experimental results at 220 VAC with COT. (a) DM noise spectrum. (b) AR.

30 kHz with QFF. It should be noted that the attenuation requirement is 40 dB/dec, therefore the headmost maximum intersected by the slash occurs at nearly 150 kHz. In conclusion, attributed to the fixed value of the operating frequency of the converter, it is very easy to find the key point for designing the EMI filter.

Figs. 28 and 29 reveal that the noises distribution is continuous with the frequency. The headmost maximum intersected by the oblique line of 40 dB/dec emerges at different frequencies

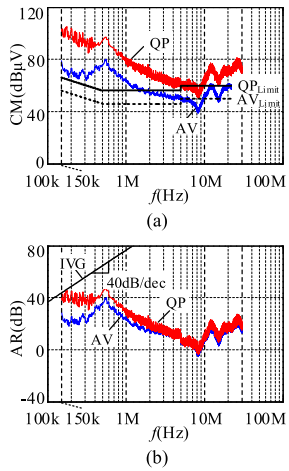

Fig. 29. Experimental results at 220 VAC with COT. (a) CM noise spectrum. (b) AR.

for differential-mode (DM) and common-mode (CM) noises. Actually, for the operation under various input voltages between 90 and 264 VAC, the case is very complicated, for the switching frequency is related to both of the rms value and the angle of the input voltage. Consequently, a lot of effort will be taken to look for the critical point and complete the design for the converter with COT.

VI. Conclusion

In this article, a QFF for CRM boost PFC converter is proposed to solve the problem of large switching frequency variation range, which has potential significance in the EMI filter design. Based on the existing research on variable on-time control, the VI is adopted to adjust the inductance to keep the switching frequency fixed at the minimum audible frequency 30 kHz in wide input voltage range. With a simple auxiliary circuit, VI can be controlled by DSP. Under the QFF control, the input PF is lowered, but the input current harmonics still well satisfy the IEC61000-3-2 Class D limits with enough margin. Meanwhile, the output voltage ripple is reduced and the efficiency is improved.

A low power is demonstrated and the work is directed at CRM boost PFC converter. Actually, VIs are suitable for high-power applications. The inductor should be redesigned, such as the core materials and type, the main winding and the auxiliary winding, the air gap, etc. Not only that, the control of the inductor must be based on the actual requirements of the converter. Of course, the control of the VI must be combined with the control of the converter itself.

High power does not mean that magnetic field intensity will increase, but depends on the selection of maximum flux density or magnetic field intensity and the operation mode of inductive current. Under the same switching frequency, the magnetic core must be larger. If the same magnetic core is adopted, the switching frequency should be larger, which depends on the specific design requirements of the converter. The difficulty of control will not increase. It is to adjust the bias current by detecting the control object. In this article, the aim is the switching frequency, while in high-power occasions, it may be other electrical quantities. The core loss and switching loss are related to many factors, such as the design index and parameters of the converter, the original intention of using VI, which is to improve the performance of the circuit or solve whatever problems, core, switching frequency, working mode of inductance current, selection of maximum flux density, selection of switch and its parasitic parameters. It can be predicted that in high-power situation, the loss must be higher than that in this article. In terms of efficiency, compared to that with fixed inductor, whether the efficiency with VI can increase or decrease is related to many factors, especially the original intention of using VI.

As far as CRM boost PFC converter with fixed switching frequency is concerned, compared to that with variable switching frequency, whether the efficiency can be improved has no direct relationship with the power level itself, but is closely related to the fixed value of frequency. If the fixed value of frequency is higher, the core loss and switching loss will be larger. The difference is that the VI needs to be redesigned when the power is higher.

It should be noted that VI needs to be designed according to the given specifications. Once the converter is operated in overload condition, the VI tends to be saturated, which is the same as that of the fixed inductor. Meanwhile, overload condition will bring higher current stress to other devices. Therefore, even if there is margin in the design, the limit should not be exceeded.

Appendix

A. Rectifier Loss

The average current value of each rectifier diode is

$$I_{\mathrm{DBR\_ave}} = \frac{1}{2\pi}\int_0^{\pi} i_{\mathrm{in}}\, d\omega t. \tag{A1}$$

KBL406 is adopted as the rectifier diode, whose conduction voltage drop $V_{F\_\mathrm{DBR}} = 0.76$ V. The conduction loss of the rectifier is

$$P_{\mathrm{DBR\_con}} = 4V_{F\_\mathrm{DBR}} I_{\mathrm{DBR\_ave}}. \tag{A2}$$

Combining (3), (4), (14), (A1), and (A2), we can get the conduction losses of the rectifier for the COT and QFF.

B. Switch Loss

Switch loss mainly include conductions loss and switching loss (turn-ON loss and turn-OFF loss).The rms value of the switch current in a switching cycle is

$$i_{Q\_\mathrm{rms}} = \sqrt{\frac{1}{T_s}\int_0^{t_{\mathrm{ON}}} i_Q^2 dt} = \sqrt{\frac{1}{T_s}\int_0^{t_{\mathrm{ON}}} \left(i_{Lb\_pk}\cdot\frac{t}{t_{\mathrm{ON}}}\right)^2 dt}$$
$$= i_{Lb\_pk}\sqrt{\frac{t_{\mathrm{ON}}}{3T_s}}. \tag{A3}$$

Then, the rms value of the switch current in a half line cycle is

$$I_{Q\_\mathrm{rms}} = \sqrt{\frac{1}{\pi}\int_0^{\pi} i_{Q\_\mathrm{rms}}^2 d\omega t}. \tag{A4}$$

FQPF4N60C is selected as the switch, whose conduction resistance $R_{ds\_\mathrm{ON}} = 1.77\ \Omega$. The conductions loss of the

TABLE III
PARAMETERS OF THE CORE MATERIAL

V_{center}(mm^3)	V_{outer}(mm^3)	A_e(mm^2)	C_m	x	y	ct_0	ct_1	ct_2	k_1	k_2
1626	3724	76	3.2×10^{-3}	1.46	2.75	2.45	3.1×10^{-2}	1.65×10^{-4}	0.01	136.4

switch is

$$P_{Q\_\mathrm{con}} = I_{Q\_\mathrm{rms}}^2 R_{ds\_\mathrm{ON}}. \tag{A5}$$

Substituting (2), (4), (7), (9), (14), (A3), and (A4) into (A5), and combining the specifications of the converter, we can obtain the conduction losses for COT and QFF.

Due to CRM, the switch features zero-current turn-ON. The switching turn-OFF loss in a switching cycle is

$$\begin{aligned} p_{q\_\mathrm{off}}(t) &= \frac{1}{2} f_s V_o i_{Lb\_pk}(t)\,\Delta t \\ &= \frac{V_m\left|\sin\omega t\right|\left(V_o - V_m\left|\sin\omega t\right|\right)}{2L_b}\Delta t \end{aligned} \tag{A6}$$

where Δt is the time required for the switch to turn OFF.

Then, the switching OFF loss in a line cycle is

$$\begin{aligned} P_{Q\_\mathrm{OFF}} &= \frac{2}{T_{\mathrm{line}}}\int_0^{\frac{T_{\mathrm{line}}}{2}} p_{q\_\mathrm{OFF}}(t)\,dt \\ &= \frac{1}{\pi}\int_0^{\pi} \frac{V_m\left|\sin\omega t\right|\left(V_o - V_m\left|\sin\omega t\right|\right)}{2L_b}\Delta t d\omega t \\ &= \frac{4V_oV_m - \pi V_m^2}{4\pi L_b}\Delta t. \end{aligned} \tag{A7}$$

The combination of (A7) and the specifications of the converter result in the switching-OFF losses for COT and QFF.

C. Output Diode Loss

The average current of the output diode is equal to the output current

$$I_{\mathrm{Db\_ave}} = I_o = \frac{P_o}{V_o}. \tag{A8}$$

MUR560 is adopted in the converter, whose conduction voltage drop $V_{F\_D} = 1.5$ V. Due to CRM, the diode has no reverse recovery. The loss is mainly the conduction one, which can be calculated as

$$P_{D\_\mathrm{con}} = V_{F\_D} I_{D\_\mathrm{ave}}. \tag{A9}$$

The substitution of (A8) into (A9) leads to the diode losses for COT and QFF.

D. Inductor Loss

As can be seen from Fig. 2, unlike the center pillar, the external magnetic circuit also contains dc bias flux. Accordingly, the core loss should be figured out separately.

According to the Steinmetz equation, the central core loss can be calculated as

$$\begin{aligned} P_{\mathrm{center}} &= \frac{10^3\,V_{\mathrm{center}}}{\pi}\int_0^{\pi} p_{\mathrm{center}} d\omega t \\ &= \frac{10^3\,V_{\mathrm{center}}}{\pi}\int_0^{\pi} C_m f_s^x \left(\frac{L_b i_{L\_pk}}{2NA_e}\right)^y \\ &\quad\times\left(ct_0 - ct_1 T_a - ct_2 T_a^2\right) d\omega t \end{aligned} \tag{A10}$$

Fig. 30. High-frequency resistance of the inductor with COT measured by the HIOKI IM3536 LCR meter. (a) At 51 kHz. (b) At 65 kHz. (c) At 100 kHz. (d) At 180 kHz.

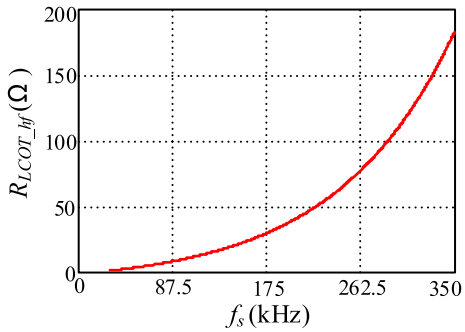

Fig. 31. High-frequency resistance of inductor versus switching frequency.

where V_{center} is the volume of central core. In the prototype, ETD29 is selected as the magnetic core, whose parameters are listed in Table III.

The outer core loss is formulated in the expression as follows [21]:

$$\begin{aligned} P_{\mathrm{outer}} &= \frac{10^3\,V_{\mathrm{outer}}}{\pi}\int_0^{\pi}\left(1 + k_1 B_{dc} e^{-\frac{L_b i_{L\_pk}}{k_2 NA_e}}\right) p_{\mathrm{outer}} d\omega t \\ &= \frac{10^3\,V_{\mathrm{outer}}}{\pi}\int_0^{\pi}\left(1 + k_1 B_{dc} e^{-\frac{L_b i_{L\_pk}}{k_2 NA_e}}\right) \\ &\quad\times C_m f_s^x \left(\frac{L_b i_{L\_pk}}{2NA_e}\right)^y \left(ct_0 - ct_1 T_a - ct_2 T_a^2\right) d\omega t \end{aligned} \tag{A11}$$

where V_{outer} is the volume of outer core, and B_{dc} is the dc magnetic flux density caused by bias current. From simulation, B_{dc} under the input voltages of 115 and 230 VAC are about

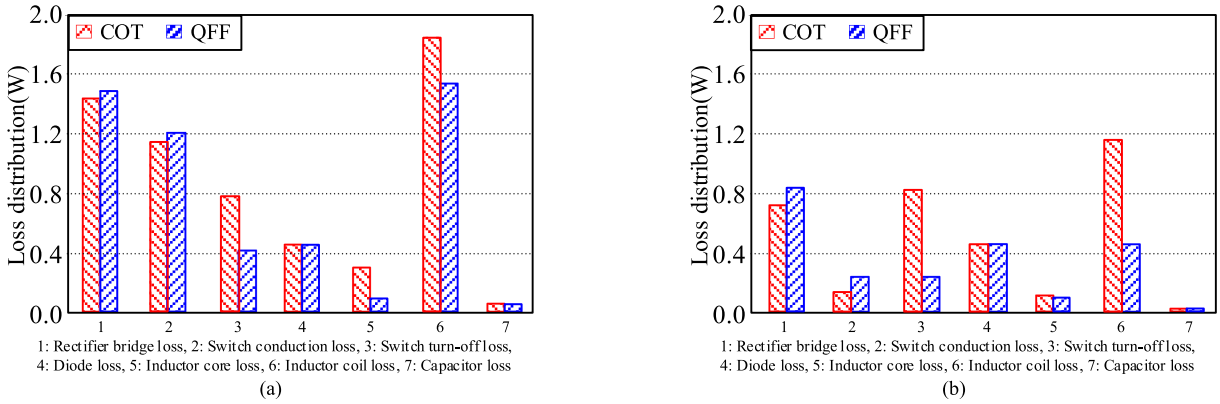

Fig. 32. Theoretical loss distribution. (a) 115 VAC. (b) 230 VAC.

400 and 85 mT, respectively. The parameters related to the core itself are shown in Table III.

The total core loss is

$$P_{\text{core}} = P_{\text{center}} + P_{\text{outer}}. \tag{A12}$$

The combination of (10), (13), (15), and (A12) yields the core losses of the boost inductor for the COT and QFF.

The rms value of the low-frequency component of the inductor current in a half line cycle is

$$I_{\text{rms\_}lf} = \sqrt{\frac{1}{\pi}\int_0^{\pi} i_{in}^2 d\omega t}. \tag{A13}$$

The rms value of the high-frequency component of the inductor current in a switching cycle is

$$i_{\text{rms\_hf}} = \sqrt{\frac{1}{T_s}\int_0^{T_s} (i_L - i_{\text{in}})^2 dt}. \tag{A14}$$

With HIOKI IM3536 LCR meter, the low-frequency and high-frequency resistances of the inductor can be measured, and $R_{\text{LQFF\_lf}} = 0.602\ \Omega$, $R_{\text{LQFF\_hf}} = 2.326\ \Omega$, and $R_{\text{LCOT\_lf}} = 0.371\ \Omega$. It should be noted that here the high frequency for QFF is 30 kHz.

For COT control, the switching frequency is continuously changing in a half line cycle. The high-frequency resistance of the inductor is different at different switching frequencies. In order to estimate the high-frequency copper loss more accurately, the resistance of the inductor for COT is measured at various frequencies every 1 kHz. Fig. 30 shows several of them. In view that the ranges of switching frequency variation at 115 and 230 VAC input voltages are 51–86kHz and 65–344 kHz, respectively, the fitting function is formulated as follows, and the curve is shown in Fig. 31

$$R_{\text{LCOT\_hf}}(f_s) = 7.86 \cdot \mathrm{e}^{\frac{f_s}{1.09\times 10^5}} - 8.41. \tag{A15}$$

Therefore, the inductor coil loss of the boost inductor is

$$P_{cu\_Lb} = I_{\text{rms\_lf}}^2 R_{L\_\text{lf}} + \frac{1}{\pi}\int_0^{\pi} i_{\text{rms\_hf}}^2 R_{L\_\text{hf}} d\omega t. \tag{A16}$$

Substituting (3), (4), (14), (A13), (A14), $R_{\text{LQFF\_lf}}$, $R_{\text{LQFF\_hf}}$, $R_{\text{LCOT\_lf}}$, and (A15) into (A16) yields the inductor coil loss for the COT and QFF.

E. Output Capacitor Loss

The loss calculation of the output capacitance is similar to that of the inductance, and it can be divided into low frequency and high frequency, which will not be discussed here.

Based on the above analysis, the theoretical loss distribution is plotted in Fig. 32.

References

[1] O. García, J. A. Cobos, R. Prieto, P. Alou, and J. Uceda, "Single phase power factor correction: A survey," *IEEE Trans. Power Electron.*, vol. 18, no. 3, pp. 749–755, May 2003.

[2] K. Raggl, T. Nussbaumer, G. Doerig, J. Biela, and J. W. Kolar, "Comprehensive design and optimization of a high power density single-phase boost PFC," *IEEE Trans. Ind. Electron.*, vol. 56, no. 7, pp. 2574–2587, Jul. 2009.

[3] X. Ren, Z. Guo, Y. Wu, Z. Zhang, and Q. Chen, "Adaptive LUT-based variable on-time control for CRM boost PFC converters," *IEEE Trans. Power Electron.*, vol. 33, no. 9, pp. 8123–8136, Sep. 2018.

[4] X. Ren, Y. Wu, Z. Guo, Z. Zhang, and Q. Chen, "An online monitoring method of circuit parameters for variable on-time control in CRM boost PFC converters," *IEEE Trans. Power Electron.*, vol. 34, no. 2, pp. 1786–1797, Apr. 2018.

[5] F. Yang, X. Ruan, Y. Yang, and Z. Ye, "Interleaved critical current mode boost PFC converter with coupled inductor," *IEEE Trans. Power Electron.*, vol. 26, no. 9, pp. 2404–2413, Sep. 2011.

[6] F. Yang, X. Ruan, Q. Ji, and Z. Ye, "Input differential-mode EMI of CRM boost PFC converter," *IEEE Trans. Power Electron.*, vol. 28, no. 3, pp. 1177–1188, Mar. 2013.

[7] Q. Ji, X. Ruan, and Z. Ye, "The worst conducted EMI spectrum of critical conduction mode boost PFC converter," *IEEE Trans. Power Electron.*, vol. 30, no. 3, pp. 1230–1241, Mar. 2015.

[8] Q. Ji, X. Ruan, L. Xie, and Z. Ye, "Conducted EMI spectra of average-current-controlled boost PFC converters operating in both CCM and DCM," *IEEE Trans. Ind. Electron.*, vol. 62, no. 4, pp. 2184–2194, Apr. 2015.

[9] K. Yao, Y. Wang, J. Guo, and K. Chen, "Critical conduction mode boost PFC converter with fixed switching frequency control," *IEEE Trans. Power Electron.*, vol. 33, no. 8, pp. 6845–6857, Aug. 2018.

[10] M. S. Perdigão, M. F. Menke, Á. R. Seidel, R. A. Pinto, and J. M. Alonso, "A review on variable inductors and variable transformers: Applications to lighting drivers," *IEEE Trans. Ind. Appl.*, vol. 52, no. 1, pp. 531–547, Jan./Feb. 2016.

[11] J. M. Alonso, G. Martínez, M. Perdigão, M. R. Cosetin, and R. N. do Prado, "A systematic approach to modeling complex magnetic devices using SPICE: Application to variable inductors," *IEEE Trans. Power Electron.*, vol. 31, no. 11, pp. 7735–7746, Nov. 2016.
[12] J. M. Alonso, M. Perdigão, G. Z. Abdelmessih, M. A. Dalla Costa, and Y. Wang, "SPICE modeling of variable inductors and its application to single inductor LED driver design, " *IEEE Trans. Ind. Electron.*, vol. 64, no. 7, pp. 5894–5903, Jul. 2017.
[13] J. M. Alonso, M. Perdigão, M. A. Dalla Costa, S. Zhang, and Y. Wang, "Analysis and experimentation of the quad-U variable inductor for power electronics applications, " *IET Power Electron*., vol. 11, no. 4, pp. 2330–2337, Nov. 2018.
[14] S. M. Ahsanuzzaman, T. McRae, M. M. Peretz, and A. Prodić, "Low-volume buck converter with adaptive inductor core biasing," in *Proc. 27th Annu. IEEE Appl. Power Electron. Conf. Expo.*, Feb. 2012, pp. 335–339.
[15] M. Beraki, M. Perdigao, F. Machado and J. P. Trovão, "Auxiliary converter for variable inductor control in a DC-DC converter application," in *Proc. 51th Int. Univ. Power Eng. Conf.*, Sep. 2016, pp. 1–6.
[16] C. Y. Lim, J. H. Kim, Y. Jeong, D. K Kim, H. S. Youn, and G. W. Moon, "A high efficiency critical mode boost PFC using a variable inductor," in *Proc. IEEE 8th Int. Power Elect. Motion Control Conf.*, May 2016, pp. 2792–2797.
[17] Y. Wei, Q. Luo, J. Wang, and S. Pengju, "Analysis and design of the DCM operation boost PFC converter with magnetic control," *IET Power Electron*., vol. 12, no. 14, pp. 3697–3706, Nov. 2019.
[18] Y. Hu, L. Huber, and M. M. Jovanović, "Single-stage, universal-input AC/DC LED driver with current-controlled variable PFC boost inductor," *IEEE Trans. Power Electron.*, vol. 27, no. 3, pp. 1579–1588, Mar. 2012.
[19] J. M. Alonso, M. S. Perdigão, M. A. Dalla Costa, G. Martínez, and R. Osorio, "Analysis and experiments on a single-inductor half-bridge LED driver with magnetic control," *IEEE Trans. Power Electron.*, vol. 32, no. 12, pp. 9179–9190, Dec. 2017.
[20] D. Medini, and S. Ben-Yaakov, "A current-controlled variable-inductor for high frequency resonant power circuits," in *Proc. IEEE Appl. Power Electron. Conf. Expo.*, Feb. 1994, pp. 219–225.
[21] A. Brockmeyer and J. Paulus-Neues, "Frequency dependence of the ferrite-loss increase caused by premagnetization," in *Proc. IEEE Appl. Power Electron. Conf. Expo.*, Feb. 1997, pp. 375–80.

Kai Yao (Member, IEEE) was born in Jiangsu Province, China, in 1980. He received the B.S. degree in industrial automation from Nantong University, Nantong, China, in 2002, and the M.S. degree in mechanical design and theory and the Ph.D. degree in electrical engineering from the Nanjing University of Aeronautics and Astronautics, Nanjing, China, in 2005 and 2010, respectively.

In 2011, he joined the Faculty of Electrical Engineering, School of Automation, Nanjing University of Science and Technology, Nanjing, China, where he has been engaged in teaching and research in the field of power electronics. His main research interests include power factor correction converters, condition monitoring, and diagnostics of power converters.

Zhen Zhang was born in Jiangsu Province, China, in 1994. He received the B.S. degree in mechanical and electronic engineering from the Jiangsu University of Science and Technology, Zhenjiang, China, in 2017, and the M.S. degree in electrical engineering from the Nanjing University of Science and Technology, Nanjing, China, in 2020.

His research focuses on power conversion technology and application, condition monitoring, and other research work.

Jian Yang was born in Jiangsu Province, China, in 1996. He received the B.S. degree in electrical engineering and automation in 2018 from Nanjing University of Science and Technology, Nanjing, China, where he is currently working toward the M.S. degree in power electronics and electric drives.

His research focuses on power factor correction the converters.

Jintao Liu was born in Fujian Province, China, in 1993. He received the B.S. degree in electrical engineering and automation in 2018 from the Nanjing University of Science and Technology, Nanjing, China, where he is currently working toward the M.S. degree in power electronics.

His research mainly focuses on power factor correction converters.

Jiazhen Li was born in Guangdong Province, China, in 1993. He received the B.S. degree in electrical engineering and automation from South China University of Technology, Guangzhou, China, in 2016. He is currently working toward the M.S. degree in electrical engineering with the Nanjing University of Science and Technology, Nanjing, China.

His main research interest focuses on power factor correction converters.

Fanguang Shao was born in Jiangsu Province, China, in 1994. He received the B.S. degree in electrical engineering and automation from Jiangsu University of Science and Technology, Zhenjiang, China, in 2019. He is currently working toward the M.S. degree in electrical engineering with the Nanjing University of Science and Technology, Nanjing, China.

His research mainly focuses on power factor correction converters.